

Shear Strengthening of Reinforced Concrete Beams Using Shape Memory Alloys

Joan M. Rius¹, Antoni Cladera^{1,*}, Carlos Ribas¹ and Benito Mas¹

(1) Department of Physics. University of Balearic Islands, Palma de Mallorca, Spain.

*Corresponding author: Antoni Cladera. Department of Physics, University of the Balearic Islands. Ctra. Valldemossa, km 7.5, Palma (Balearic Islands), Spain. Phone number: +34 971 17 1378. E-mail: antoni.cladera@uib.es

Abstract

Shear failures in RC members are associated with brittle collapses, for this reason, shear strengthening of existing structures is often required. This paper presents an innovative system for retrofitting shear critical reinforced concrete (RC) beams, taking advantage of the shape memory effect of shape memory alloys (SMAs). The new system uses the SMAs as active external reinforcement thanks to the recovery stresses that SMAs are able to generate during their activation under restrained strain. An experimental campaign has been carried out on small-scale RC beams with rectangular cross-section (80-mm wide and 150-mm deep) strengthened in shear by means of 3 mm diameter Ni-Ti-Nb wires externally installed around the beams, forming a pseudo-spiral, in order to actively confine, or transversally prestress, the RC members. The experimental results show an increase of the shear strength around 90 % and 115 % of the retrofitted beams depending on the strengthening configuration, and also a more ductile shear failure. The effect of the geometrical imperfections occurred during the installation of the external reinforcement has been studied, and the possible prestressing losses due to these imperfections have also been evaluated. It has been concluded that the Ni-Ti-Nb wires show a promising performance despite possible imperfections in small-scale members. Finally, a previously developed shear model has been used to predict the shear strength of the tested beams. The recovery stresses considered for the pseudo-spirals were derived from separate material tests simulating similar imperfections. The predictions given by the shear model are satisfactory, with an average value of the ratio V_{test}/V_{rd} equal to 1.14 and a coefficient of variation of 8.4 %.

Keywords: Ni-Ti-Nb; shape memory alloy; shape memory effect; shear strength; reinforced concrete; strengthening.

1. Introduction

Shear failures in reinforced concrete (RC) members are associated with brittle collapses, which may cause sudden material and human losses. It is obviously necessary to avoid this type of failure, usually through the shear strengthening of existing structures. Strengthening is often needed to address deficiencies of various causes, e.g. design mistakes, changes in the use of a structure, or new code requirements.

The strengthening technologies for critical shear beams may be classified into two categories: passive and active strengthening methods. In the passive methods, the deformation of the strengthened structure is needed to increase and to reach a certain level of damage before the strengthening material can begin to contribute. On the other hand, in the active methods, the strengthening material immediately begins working upon installation. Different researches focused on passive strengthening methods have been previously published: using external CFRP strips [1], by means of self-compacted concrete jacketing [2], with externally bonded FRP fabric [3], or steel fiber reinforced concrete [4]. Other works have focused on active strengthening methods using vertical prestressed clamps reinforcement [5], or by means of prestressed wire ropes [6] or tendons [7]. The advantages of an active FRP shear strengthening system are summarized by Motavalli et al. [8]: a) failure loads and deformations at failure are higher, b) the width of existing shear cracks and stresses in internal steel stirrups, if exists, can be reduced, c) there exists an immediate reaction to additional loads, d) a better utilization of the strengthening material can be achieved. However, in both cases, the strengthening increases the safety of the structure and its strength for future applications of load, but when using passive strengthening methods, as previously commented, it is necessary for the strengthened structure to increase its deformation and level of damage before engaging the strengthening material. Alternatively, part of the load must be removed before placing the strengthening material (e.g. by shoring), and then, the strengthening material can contribute as soon as additional load is applied (or shoring removed). When using active strengthening methods, the structure is prestressed or actively confined when the strengthening material is placed [7]. However, active strengthening methods generally require hydraulic jacks and anchorages, so it is often necessary to maintain a large work area to accommodate these auxiliary elements. Moreover, regarding the active strengthening system using FRP presented in [8], the authors stated that several innovative ideas had been successfully realized in the laboratory, with encouraging

results, although practical and theoretical problems remained to be solved before these techniques could be fully applied.

In terms of structural engineering, shape memory alloys (SMAs) have three key properties: shape memory effect (SME), pseudoelasticity, and damping capacity. The SME, an essential property for the featured strengthening technology, refers to the phenomenon whereby SMAs are capable of returning to a predefined shape upon heating. If this recovery strain is constrained because the SMA is used, for example, to wrap a beam, the SMA will generate recovery stresses when heated and cooled afterwards, prestressing and/or confining the concrete member. With the adequate selection of the SMA, these stresses will remain applied throughout the service life of the structure, even though higher levels of stress relaxation than in conventional steel can occur, at least when using iron-based SMAs [9]. Some of these SMAs also possess a very high ductile behavior, for example some iron-based SMAs present strains at failure higher than 40 % [10] or the Ni-Ti-Nb alloy used in this research with strains at failure around 37%, as will be seen later. This ductile behavior of the SMAs has been found to be essential for providing ductile shear failures when used as internal reinforcement [11].

Binary Ni-Ti alloys are the current market-dominant alloy, with many applications across different fields, such as aviation, surgical medical equipment, and implants [12]. Ni-Ti alloys have also been used in many civil engineering applications, due to their pseudoelastic behavior and their damping capacity: wires for dampers and actuators [13], cables for reinforced concrete applications [14], or bars under compression [15], among many others. However, its narrow thermal hysteresis make this alloy inappropriate for use in prestressing applications in civil engineering structures relying on the shape memory effect [16]. Ni-Ti-Nb alloys were first reported in 1986 [17,18] and they are easier to handle and store owing to their larger temperature hysteresis. This allows the material to be prestrained at a low temperature, to be safely transported at ambient temperatures, to be activated at a higher temperature, and to retain high values of recovery stresses at ambient temperatures.

Ni-Ti-Nb wires have been successfully used to actively confine circular and non-circular columns to improve their behavior under axial compression forces and bending [19–21]. However, the application of this material for shear strengthening has not been deeply investigated. Even though SMA rods have been used as shear repair system for a concrete bridge girder [22], there have not been reported, to date, RC tests using SMAs

with recovery stresses above 400 MPa for shear strengthening, to the best of the authors' knowledge.

In this paper, an experimental campaign on 10 small-scale beams will be reported. Eight of these beams has been externally strengthened using 3 mm diameter Ni-Ti-Nb wires. The Ni-Ti-Nb wires have been completely characterized, including their shape memory effect and their recovery stress generation capacity. The wires introduced an active transversal prestressing force into the retrofitted beams after heating them. The effect of the geometrical imperfections occurred during the installation of the external reinforcement has also been studied, evaluating the prestressing losses. Finally, the Compression Chord Capacity Model is presented as a recent developed shear model, and it is used to satisfactorily predict the shear strength of the reference and the retrofitted beams.

Note that the recent commercialization of iron-based shape memory alloys specially designed for the construction sector [10][22], with a significant lower cost than the SMA used in this paper, will probably bring the use of SMAs to the construction market on real engineering projects. Some parts of the methodology outlined in this paper may be common to the shear strengthening of RC beams using different SMAs.

2. Fundamentals of the martensitic transformation focusing on the shape memory effect

The martensitic transformation is a diffusionless, solid state displacive transformation in which the atoms move cooperatively. It is normally accompanied by shear stresses that deform the structure homogeneously and give rise to a change in the crystal structure as well as the associated volume [12]. The new phase is constituted through small, coordinated displacements of the atoms, where the displacements of neighboring atoms are smaller than their original interatomic distances. Martensitic transformation takes place through the lattice deformation that modifies the crystal structure of the parent austenite phase to the martensite phase but the deformation mechanism is different from the slip of crystals by dislocations [23]. Fig. 1a shows schematically the atomic arrangement in a hypothetical lattice after mechanically induced martensitic transformation. The lattice is distorted without reorganization of the atoms (neighbors stay neighbors). In a plastic deformation, on the other hand, the atoms are rearranged by slip, as shown in Fig. 1b. In this case, the neighbors are changed, but the lattice structure remains intact. This transformation can

occur in a general alloy or in an SMA for high strains, and cannot be reversed by a temperature change because the crystal structure is identical to the original state [22].

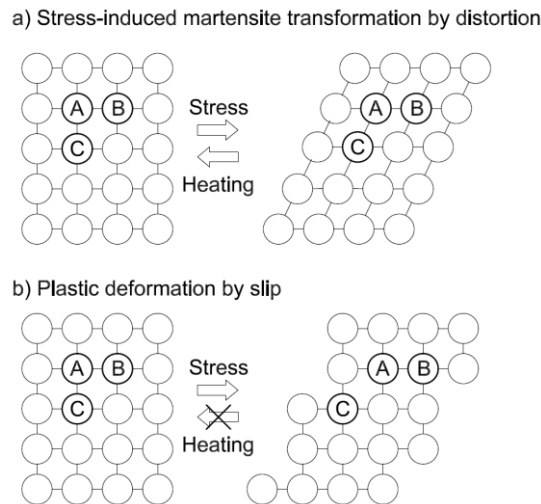


Fig. 1. Different atomic behaviors of: a) stress-induced martensitic transformation by distortion in Ni-Ti; b) plastic deformation by slip. Adapted from [23].

Although the variation in the relative position of the atoms is very small in the martensitic transformation, the coordinated movement of all the atoms leads to changes in volume and may bring about significant macroscopic deformations. In this research, the transverse prestressing effect of the strengthening spiral is obtained by means of the reverse martensitic transformation produced by an increase in temperature, producing macroscopic deformations trying to shorten the SMA. The martensitic transformation takes place within a finite interval of temperatures (Fig. 2), during which there is a coexistence of the two phases: austenite and martensite.

The martensitic transformation, or forward transformation, is induced upon the cooling of the austenite phase (a highly symmetric cubic phase, with the existence of only one single possible structure in this case, which is stable at high temperatures) and consists of the appearance of the martensite phase (a low-symmetry phase stable at low temperatures, with different configurations or variants: up to 24 for Ni-Ti). In the absence of applied stresses, the temperature at which the process begins is defined as M_s (martensite start), and M_f (martensite finish) is the temperature at which the transformation finishes. The assembly of martensitic variants can exist in two forms in Ni-Ti: twinned martensite, which is formed by a combination of self-accommodated martensitic variants, and detwinned martensite, in which a specific variant is dominant [24].

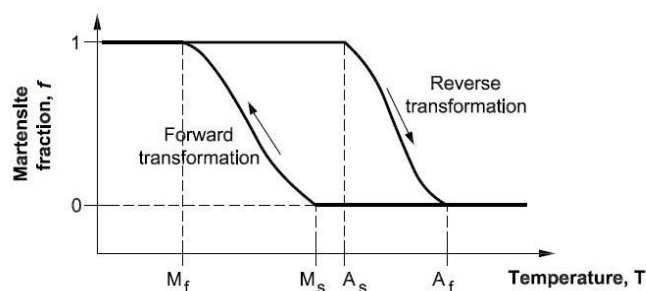


Fig. 2. Schematic of phase transformation in SMAs according to temperature. Adapted from [22].

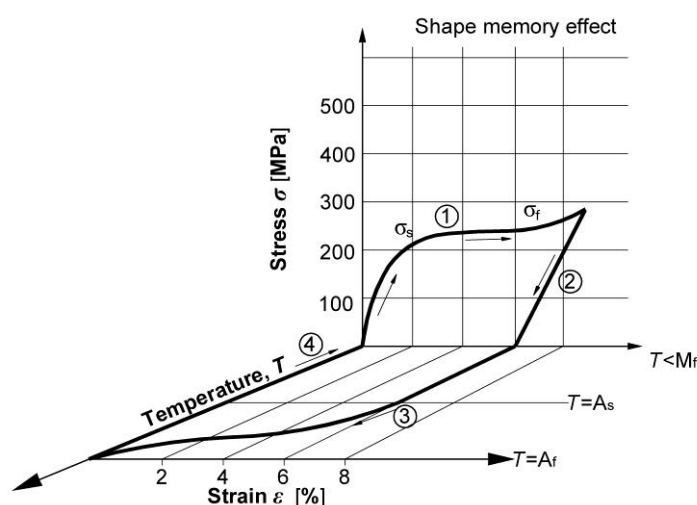


Fig. 3. Shape memory effect. Typical stress-strain-temperature diagram. Adapted from [25].

If the temperature is appropriate for the material to be in the martensite phase ($T < M_f$), the reverse transformation can be induced by heating the material. Using similar terminology to the martensite phase, the formation of austenite begins at temperature A_s (austenite start) and will finish at temperature A_f (austenite finish), see Fig. 2.

The shape memory effect occurs when deformations due to an applied stress (which produced martensite) are recovered by heating the material above A_f [25]. Figure 3 presents a typical stress–strain–temperature diagram summarizing the shape memory effect. If the initial temperature of the SMA is lower than M_f , the SMA will be in the martensite phase. In this situation (initially twinned martensite), it is possible to detwin the martensite (Path 1 in Fig. 3). In this step, the applied stress must be sufficiently large (σ_s) to start the detwinning process. The total detwinning of martensite is reached at the detwinning finish stress (σ_f). After reaching σ_f , the alloy starts another elastic phase with the initial modulus of elasticity of the martensite. After unloading (Path 2 in Fig. 3), the martensite remains detwinned. The change in phase from detwinned martensite to

austenite can be brought about by raising the temperature (Path 3 in Fig. 3), causing the SMA to regain its cubic crystal structure and returning it to its original shape if the deformations are unconstrained (Path 4 in Fig. 3). If the deformation is impeded (a scenario not represented in Fig. 3), the SMA will generate recovery stresses when heated. During the prestraining represented by Path 1 in Figure 3, it is important not to keep loading after the elastic branch of the martensite. If the stress were to continue increasing after that elastic branch, a plastic branch of martensite would be produced that is irrecoverable upon unloading or heating it, a phenomenon not represented in Fig. 3.

Different thermal hysteretic behavior of constrained SMAs can involve great differences in the development of recovery stresses [22], as can be seen in figure 4 that shows the schematic stress–strain diagrams and thermomechanical paths during the heating and subsequent cooling of two constrained SMAs: a narrow hysteresis alloy (Ni-Ti) and a wide hysteresis alloy (Ni-Ti-Nb).

The prestraining follows Path 1 from Fig. 3, starting with twinned martensite material and evolving into an almost horizontal plateau, in which the detwinning process takes place. For Ni-Ti alloys, the recovery stress increases during heating but significantly decreases during subsequent cooling due to forward transformation (Path 4 in Figs. 4a and 4c). For Ni-Ti-Nb alloys (Figs. 4b and 4d), which have a larger hysteresis, it is entirely possible to maintain the recovery stresses after returning to the ambient temperature (AT). Note that Paths 3 and 4 in Fig. 4 (for the constrained specimen, indicating the generation of recovery stresses) are different than Paths 3 and 4 in Fig. 3 (for the unconstrained specimen, indicating strain recovery).

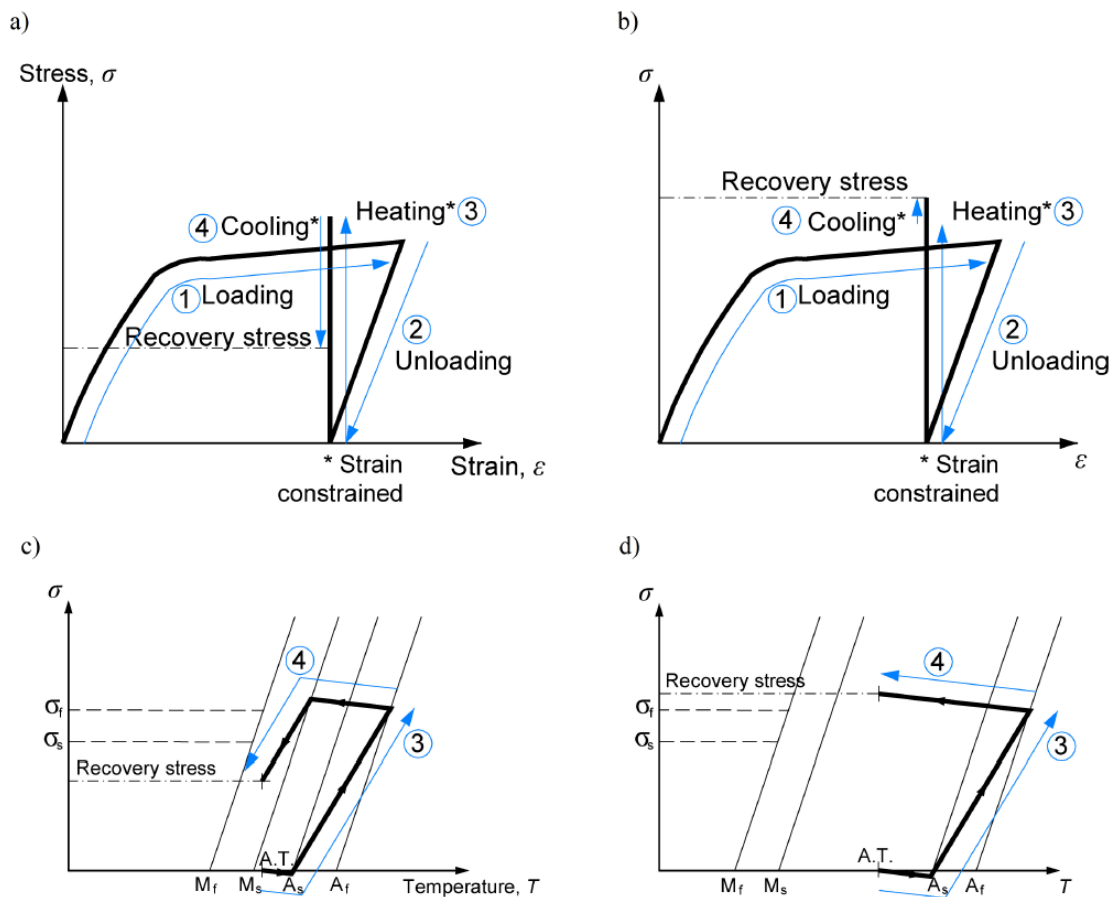


Fig. 4. A and b) Schematic stress-strain diagrams of prestraining and generation of recovery stresses during activation: a) Narrow hysteresis alloy (Ni-Ti); b) Wide hysteresis alloy (Ni-Ti-Nb). C and d) Schematic thermomechanical paths during the heating and cooling: c) Narrow hysteresis alloy (Ni-Ti); d) Wide hysteresis alloy (Ni-Ti-Nb). Adapted from [22].

3. Experimental program

3.1 Design of the test specimens

An experimental program was designed to test different shear strengthening configurations. Ten small scale RC beam specimens without transverse reinforcement were produced, all with the same geometry and longitudinal reinforcement. The 10 beam specimens, as well as the test cubes and test cylinders for the determination of concrete compressive and splitting strength, were cast from a single concrete batch. The desired concrete compressive strength was 40 MPa. The RC beam specimens were 80-mm wide (b), and 150-mm deep (h), as shown in Fig. 5. The total length of the beam specimens was 900 mm, and the tests were carried out by loading the beams at a central point, testing both sides identically and at the same time. The shear span, a , was equal to 340

mm, with a/d approximately equal to 2.68, where d is the effective depth of the beams ($d = 127$ mm). The characteristics of the beam specimens are summarized in Table 1.

The shear strengthened specimens, and the test procedures, had different configurations: different spiral pitch, tests carried out before or after wire activation, and different previous loading history (intact beams, pre-cracked beams, or beams preloaded up to failure). Reference specimens without shear reinforcement were also tested. The test procedure for the preloaded beams was: a) placement of the non-activated wire (with initial imperfection); b) application of the preload (until failure for beams 3.1 and 3.2, and until the development of the first branch of the critical crack in the case of beams 4.1 and 4.2); c) beam unloading; d) activation of the wires; and e) reloading up to failure. The nomenclature for the different beam specimens (e.g., 2.1 - S ϕ 3/100/UCR/A) is as follows: the nomenclature begins with a short test code (1.1 to 5.2) for fast identification. If this code is followed by “a” or “b”, it means that the beam specimen was tested twice, “a” indicating the first test. Next, S ϕ 3 (3-mm diameter spiral) indicates the type of shear strengthening used, followed by “100” or “075”, indicating the pitch in mm of the Ni-Ti-Nb pseudo-rectangular spiral. Note that the external shear reinforcement has two different inclinations as it is a pseudo-rectangular spiral: on one side the angle between the axis of the beam (horizontal axis) and the links is 90°, and on the other side the angle is 56° or 63° depending on whether the pitch is 100 or 75 mm, respectively (Table 1, Fig.5a). Note also that the pseudo-rectangular spiral pitch near the point of load application is reduced so that it does not overlap with the load application plate (Fig. 5a). The next field consists of three letters, “UCR”, “PCR” or “COL”, indicating that the beam specimen was uncracked when the strengthening spiral was placed and activated (UCR), that it had been previously loaded until a shear crack appeared (PCR), or that the beam specimen had already been tested until collapse, and, after the collapse, the strengthening spiral had been activated (COL). The last term indicates whether the strengthening spiral had been activated before the beam test (A), or had been placed but not activated before the beam test (NA). To ensure the repeatability of the findings, two identical beams were tested for each set of criteria (for example, Beams 2.1 and 2.2, where the second number indicates the first and the second beam specimen tested).

In real engineering practice, the objective of strengthening a RC beam in shear would be to avoid the shear failure, forcing the shear strength to be higher than the flexural strength and, consequently, inducing a more ductile flexural failure. However, to be able to quantify the shear strengthening effect with the proposed technology, the objective

during the design of the experimental campaign presented in this paper was to raise the shear strength but without reaching the flexural strength.

Table 1. Details of the beam specimens.

Beam no.	Age at testing (days)	f_{cm} (MPa)	f_{sp} (MPa)	Shear strengthening			Comments	
				ϕ /spacing (mm)	Ni-Ti-Nb state	ϕ_{front} (°)		ϕ_{back} (°)
1.1 – Reference	49	41.4	3.2	-	-	-	-	
1.2 – Reference	56	41.7	3.2	-	-	-	-	
2.1 - S ϕ 3/100/UCR/A	63	41.9	3.2	ϕ 3/100	Activated	90	56	Un-cracked
2.2 - S ϕ 3/100/UCR/A	68	42.1	3.2	ϕ 3/100	Activated	90	56	Un-cracked
3.1a - S ϕ 3/100/UCR/NA	102	42.6	3.3	ϕ 3/100	Non-Activated	90	56	Un-cracked
3.1b - S ϕ 3/100/COL/A	130	42.8	3.3	ϕ 3/100	Activated	90	56	Tested after collapse 3.1a
3.2a - S ϕ 3/100/UCR/NA	102	42.6	3.3	ϕ 3/100	Non-Activated	90	56	Un-cracked
3.2b - S ϕ 3/100/COL/A	116	42.7	3.3	ϕ 3/100	Activated	90	56	Tested after collapse 3.2a
4.1 - S ϕ 3/100/PCR/A	175	43.0	3.3	ϕ 3/100	Activated	90	56	Pre-cracked V_{cr} =17.79 kN
4.2 - S ϕ 3/100/PCR/A	182	43.0	3.3	ϕ 3/100	Activated	90	56	Pre-cracked V_{cr} =18.08 kN
5.1 - S ϕ 3/075/UCR/A	263	43.2	3.4	ϕ 3/75	Activated	90	63	Un-cracked
5.2 - S ϕ 3/075/UCR/A	272	43.2	3.4	ϕ 3/75	Activated	90	63	Un-cracked

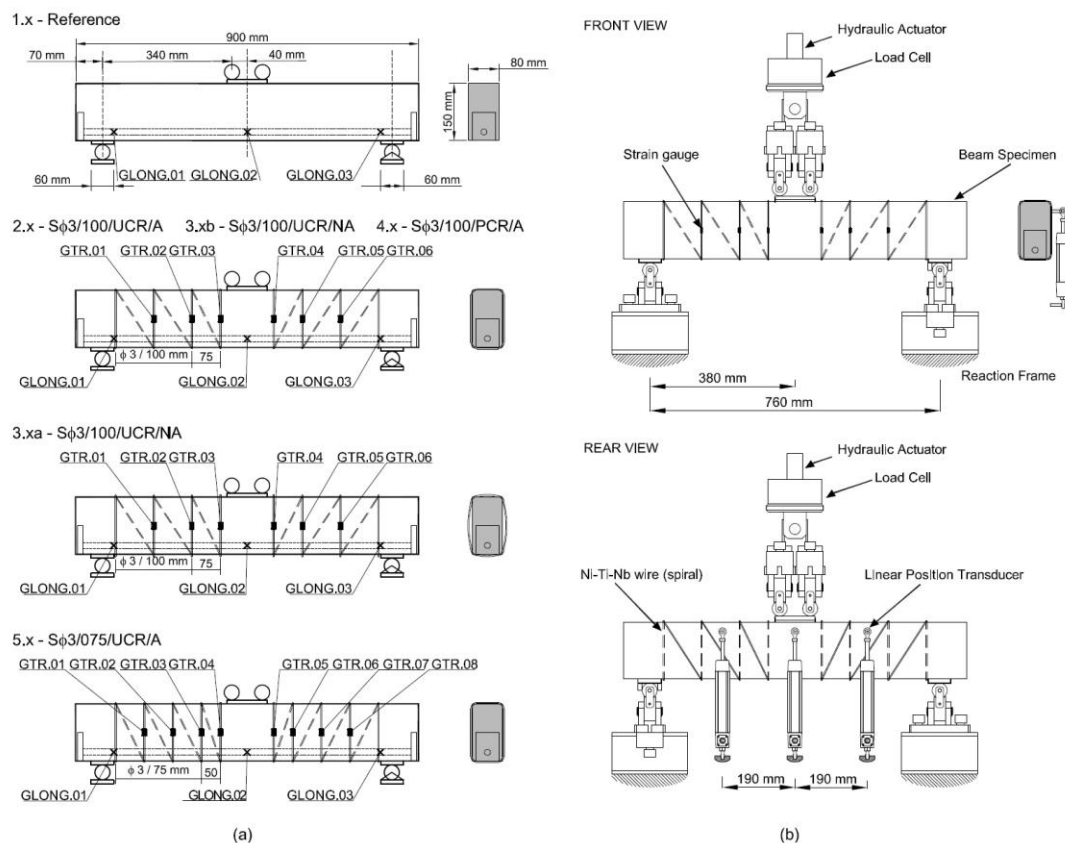


Fig. 5. a) Beam geometry and strain-gauge positions. b) Test set-up.

3.2 Fabrication of the test specimens: concrete and steel properties

The beams were cast at a precast concrete plant. A maximum aggregate size of 14 mm was used. Standard 150-mm cubes and 150 mm × 300 mm cylinders were cast with the

specimens to obtain the compressive strength, f_{cm} , and the splitting strength, f_{sp} , respectively. These cubes and cylinders were kept under the same environmental conditions as the beam specimens, in the laboratory with a temperature typically around 20 °C, until the time of testing of the beams. The f_{cm} and f_{sp} estimations given in Table 1 are derived from the results of 23 cube tests for the compressive strength and 25 cylinder tests for the splitting strength, in compliance with UNE-EN-12390-3 Standard [26] and UNE-EN-12390-6 Standard [27] respectively, tested at 28 days (in compliance with EHE2008 Code [28]) and at the age of each beam specimen at the time of testing.

Longitudinal reinforcement was composed of $\phi 16$ mm standard B500SD rebars ($A_s = 201 \text{ mm}^2$). Both ends of the bars were welded to a plate to guarantee sufficient anchorage in such small beam specimens. The mechanical properties of the longitudinal bars, obtained in compliance with UNE 36065 Standard [29], are: $f_y = 513 \text{ MPa}$, $f_u = 642 \text{ MPa}$, $\varepsilon_u = 20.5\%$ (mean value of two tests reported).

3.3 Ni-Ti-Nb characterization

For the external shear strengthening, 3 mm-diameter Ni-Ti-Nb wires without ribs or indentations of any type were used. A Ni-Ti-Nb sample was analyzed through energy dispersive X-ray spectroscopy (EDX) to determine its composition, establishing the Ti content at 45.81 at%, the Ni content at 45.76 at%, and the Nb content at 8.43 at%.

Fig. 6 shows the results of the Differential Scanning Calorimetry (DSC) carried out on the Ni-Ti-Nb alloy to determine its phase transformation temperatures. These temperatures are estimated by studying the variations in the amount of heat required to increase the temperature of the sample. From the DSC, the detected phase transformation temperatures were $A_s = 72 \text{ °C}$ and $A_f = 85 \text{ °C}$. Martensite start and finish temperatures were not detected in the performed DSC (as the minimum temperature was -100 °C for the equipment used), so electrical resistance tests were carried out to determine these phase transformation temperatures. The experimental technique employed four wire alternating current (ac) impedance measurements at a frequency of 686 Hz [30]. The real part of the impedance R was measured by means of a lock-in amplifier, which provided high resolution measurements. The available temperature range was -190 °C to 120 °C . The transformation temperatures measured with this technique are shown in Fig. 7a: $M_f = -135 \text{ °C}$, $M_s = -105 \text{ °C}$, $A_s = 69 \text{ °C}$ and $A_f = 74 \text{ °C}$. A second thermal cycle was carried out (Fig. 7b), obtaining the same M_f and M_s temperatures, but different values of $A_s = -45 \text{ °C}$ and $A_f = -21 \text{ °C}$. These results are coincident with the reported wide thermal hysteresis of

Ni-Ti-Nb for the first thermal cycle. The observed reduction of the austenitic phase temperatures in the second cycle is not considered detrimental for the use of this alloy in this application, but beneficial, as once the SMA has been transported to the working place, installed, and activated, the alloy will remain in its austenite phase, except if ambient temperatures decrease to $-100\text{ }^{\circ}\text{C}$, a scenario not envisaged for most civil engineering structures. Furthermore, as the austenite start temperature, A_s , is around $70\text{ }^{\circ}\text{C}$, the prestrained wires may be safely stored, transported, and installed without risk of accidentally induce the reverse transformation (Fig. 2) if the temperature is kept lower than $70\text{ }^{\circ}\text{C}$.

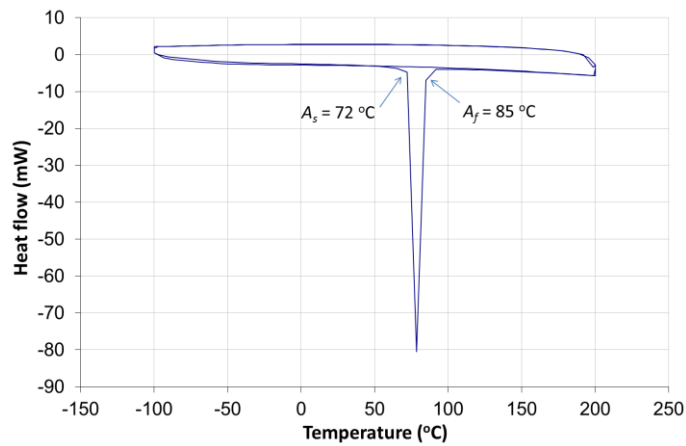


Fig. 6. Differential Scanning Calorimetry (DSC) of Ni-Ti-Nb.

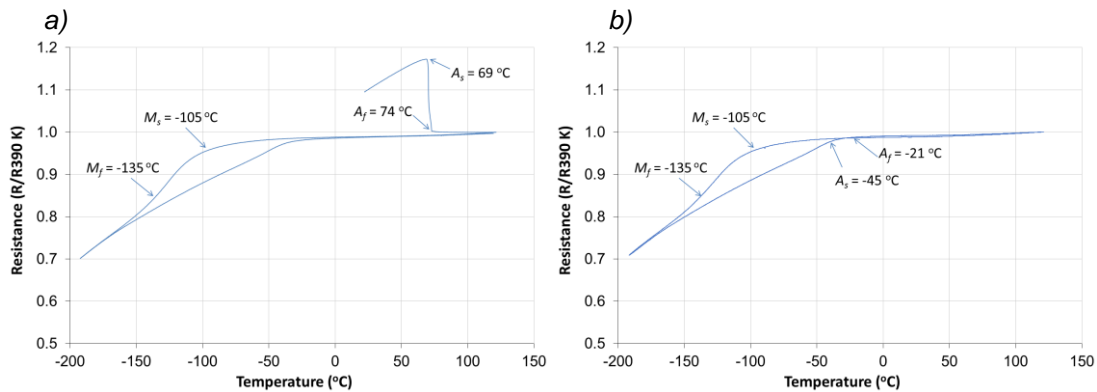


Fig. 7. Temperature dependence of resistance for a Ni-Ti-Nb sample. Data are normalized to the value of resistance at 390 K. a) First cycle. b) Second cycle.

All stress–strain–temperature experiments on the Ni-Ti-Nb wire samples were conducted on a Zwick load frame with a capacity of 100 kN. To control the samples' temperature, a thermal chamber was used when required. The length of the standard

sample was 150 mm between clamps, plus 75 mm inside each clamp. The experiments were performed at a displacement rate of 7.5 mm/min.

The stress–strain curve of the Ni-Ti-Nb wire as provided by the manufacturer (6 % prestrained) is shown in Fig. 8 as a representative result of the material behavior in martensite phase at RT. The ultimate strength is approximately equal to 1000 MPa for a strain of around 37% (Fig. 8). The modulus of elasticity calculated at stresses between 100 and 350 MPa, is equal to 25 GPa.

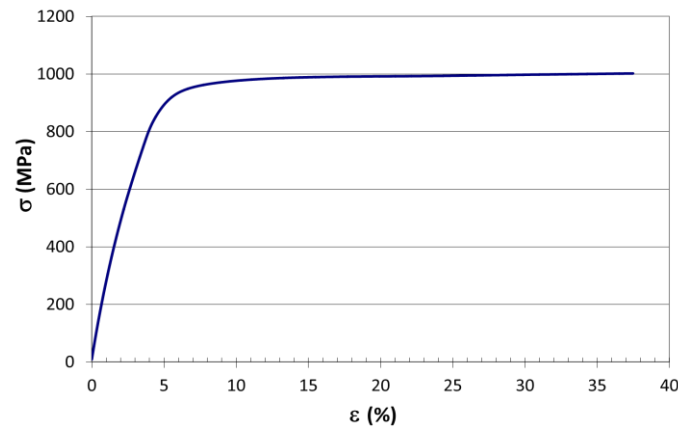


Fig. 8. Stress–strain behavior at Room Temperature of Ni-Ti-Nb as provided by the manufacturer (martensite).

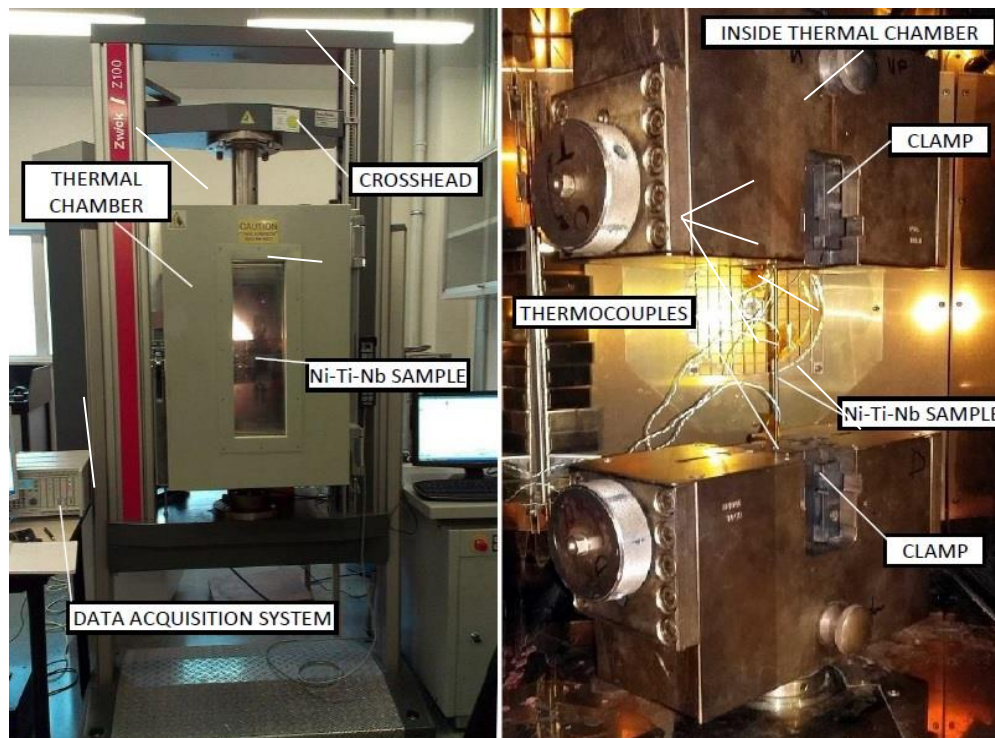


Fig. 9. Experimental set-up for recovery stress test.

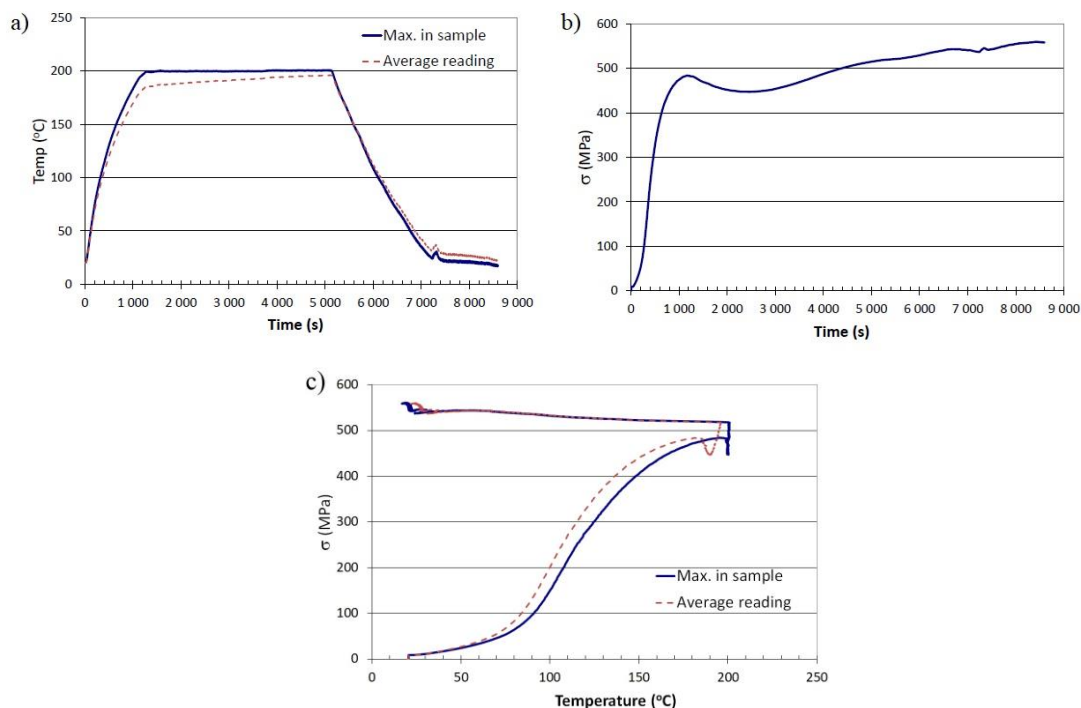


Fig. 10. Stress recovery test: a) Temperature vs. time. b) Stress vs. time. c) Stress vs. temperature. Blue line: maximum temperature in the sample. Red dashed line: average of the temperature readings of 3 attached thermocouples.

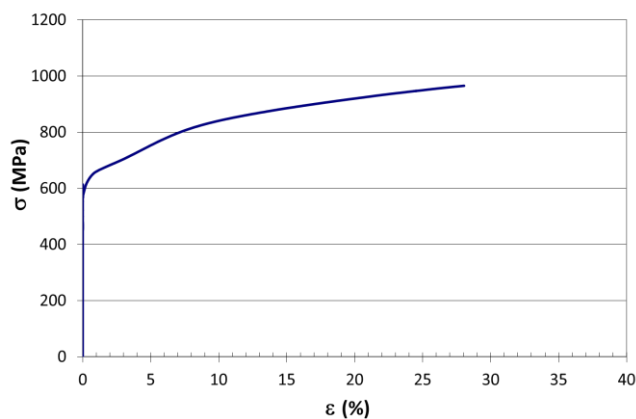


Fig. 11. Stress–strain behavior at Room Temperature of the Ni-Ti-Nb after stress-recovery test.

Figure 9 shows the test set-up to perform a stress recovery test. In this test, the Ni-Ti-Nb sample is heated in the thermal chamber up to 200 °C, the temperature is kept constant, and then the chamber is cooled. The test is performed controlling the position of the crosshead, after an initial pre-load of around 8 MPa. During the test, the load cell measures the stresses generated to keep the position of the crosshead constant. Note that while this test is performed, the deformation of the sample is prevented avoiding the movement of the crosshead. Since the sample has a tendency to shorten due to the inverse

martensitic transformation when it is heated (Fig. 10a), tensile stress in the sample increases (Fig. 10b). Buckling is therefore not possible after activation. Nine different stress recovery tests were carried out heating the sample to 200 °C and cooling it afterwards in the thermal chamber. Figure 10 depicts the results of a representative stress recovery test with obtained recovery stress value of 560 MPa. Three thermocouples were placed along the sample (close to the clamps and in the center) to verify that the desired temperature was reached throughout the sample. It was considered after 5000 seconds that the temperature was practically constant in all the sample, see the average of the readings of the 3 thermocouples and the maximum temperature in Fig 10a, and that the inverse transformation had already took place. Afterwards, the temperature was decreased to RT. After performing the recovery stress test, and without unloading the sample, a conventional stress-strain test was performed, with the results shown in Fig. 11. In this situation, the ultimate stress was approximately 965 MPa for a strain of around 28% (Fig. 11). The tangent modulus of elasticity at the beginning of the tensile test after activating the SMA with constrained strain (with the initial stress of the tensile test at around 560 MPa, see Fig. 11) was 25 GPa, although the modulus decreased above a stress of 650 MPa.

In the recovery stress test represented in Fig. 10, the sample is perfectly straight before heating, which is carried out inside the thermal chamber. However, the heating of the strengthening wires placed around the beams is carried out using a heat gun. Moreover, during the strengthening of the beams, some inevitable imperfections occur, and the initial length of the spiral links may be slightly greater due to some initial curvature of the wire wrapping the beams (Fig. 12c). For this reason, recovery stress tests with different initial degrees of imperfection due to curvature were performed (Fig. 12a and Fig. 13). The test labeled as straight in Fig. 13a was carried out without initial imperfection to compare with other tests with initial imperfections ranging from 0.5 % to 6 % of extra initial length. For clarity, only tests up to 2.34 % are shown in Figure 13a. Figure 13a shows the stress-time curves of the three tests with the least imperfections, as the actual imperfection produced in the wires when they were placed around the beams were between 0.54 % and 2.34 %.

Figure 13b shows the test results of the final recovery stress (see right hand side of Fig. 13a). An approximate safety-side performance curve $\sigma_R(i_0) = -7.6829 i_0^2 + 443$ has been derived, where σ_R is the recovery stress and i_0 is the percentage of initial imperfection. In all the beam tests, it was ensured that the maximum imperfection before the activation of

the external reinforcement was less than 1.9 %. This initial imperfection disappeared during activation (Figures 12b-d). Therefore, based on the proposed curve shown in figure 13b, and knowing that the maximum imperfection in the beams is 1.9 %, a recovery stress of 415 MPa will be adopted for design. Note that the result of the test using the straight sample in Fig. 13 is different from the results of the test shown in Fig. 10. The recovery stress in the test with the straight sample in Fig. 13 is lower, since it was activated by means of a heat gun. A non-perfect heating and time-dependent strains may have affected those results. In any case, the values of recovery stresses to be used for the prediction of the shear strength will be those derived considering the initial imperfection and the activation with a heat gun.

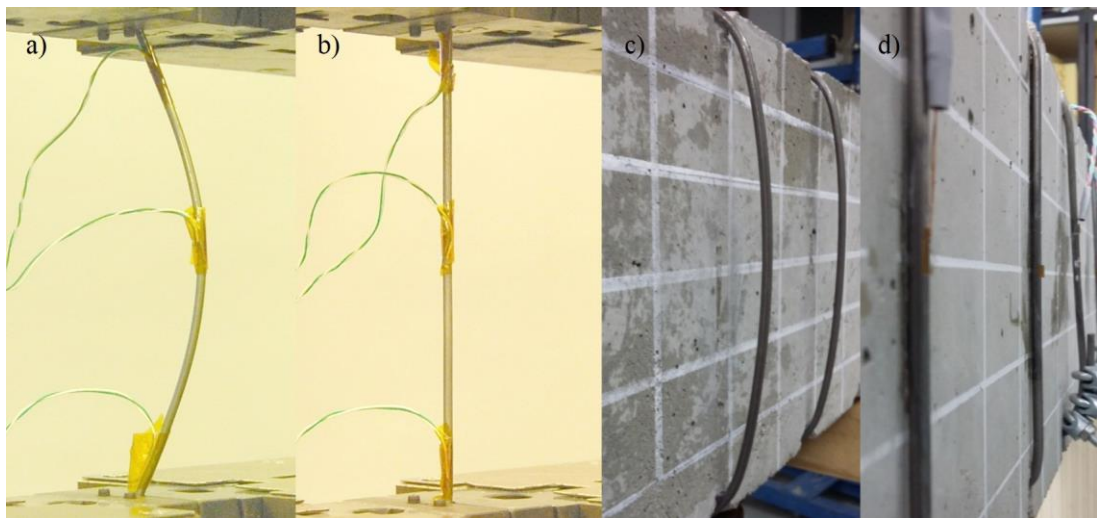


Fig. 12. Initial imperfection (curvature) before activation of SMA at tensile test (a) and on a beam (c) and after activation (b and d).

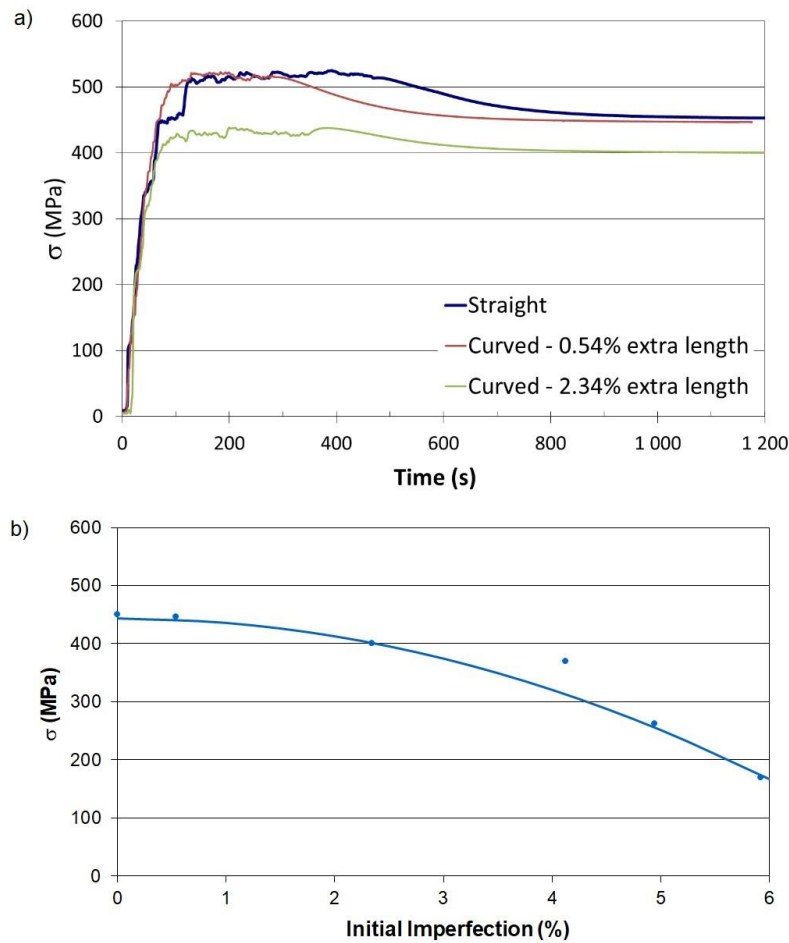


Fig. 13. a) Stress recovery tests with initial imperfection. b) Recovery stress-initial imperfection.

3.4 Strengthening of the beam specimens

The prestrained Ni-Ti-Nb wire was wrapped around the beam specimens (Fig. 14a). The wire was placed vertically on the front side ($\varphi_{front}= 90^\circ$ in table 1) and inclined on the back side ($\varphi_{back}= 56^\circ$ for pitch equal to 100 mm in table 1). Note that small and short grooves were made at the corners of the rectangular cross-section, to ensure a proper rotation of the wires and to minimize the initial imperfections during their placement. The anchoring of the wires was performed using two different configurations: the external end of the wire was anchored to the concrete by means of bolts and a small steel plate (Fig. 14d); the internal end of the wire was self-anchored by means of U-bolt saddle clamps (Fig. 14c). The placement of the wire into the small grooves at the corners avoided the slippage of the wires during the activation. The spiral was activated afterwards using a heat gun (Fig. 14b), heating the wires from the external corners towards the web mid-height, producing the reverse martensitic transformation. Since the slippage of the wires

was avoided, as it was visually observed during the process and previously commented, the sequential activation procedure with the heat gun ensured the development of the recovery stresses. Moreover, the temperature in the wire was monitored during the activation by means of thermocouples, reaching always 200 °C. As a result, the Ni-Ti-Nb wire attempted to be shortened but was restrained because of the presence of the beam around which it was wrapped. Thus, the wire transmitted the stresses induced by its transformation to the beam in the form of confining stresses. The use of external spirals was chosen because the spiral geometry had already shown important benefits as internal reinforcement for shear, using common materials or even shape memory alloys [11,31–34].

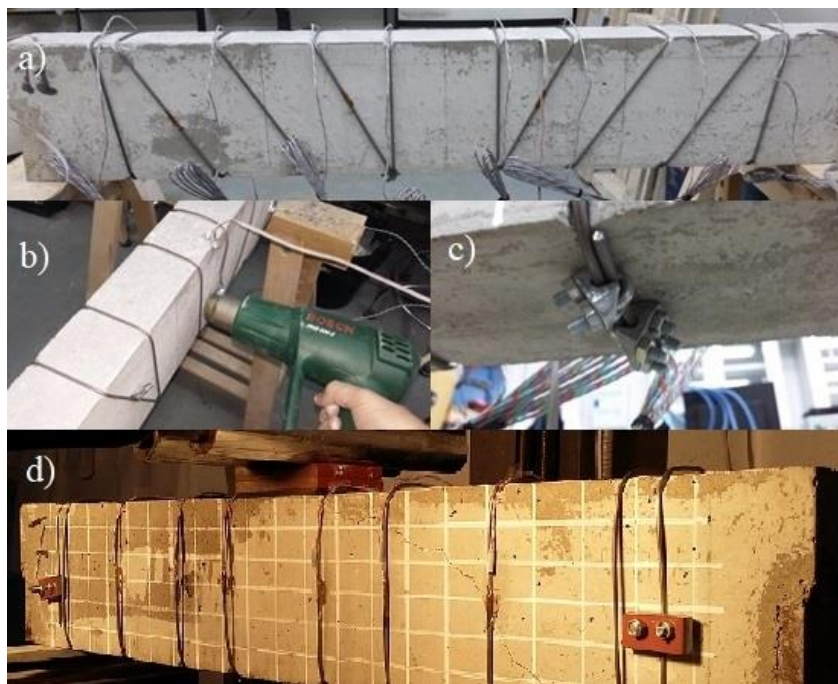


Fig. 14: a) Rear view of a strengthened beam, b) activation process by means of heat gun, c) detail of the anchoring using U-Bolt saddle clamps, and d) front view of a beam with left and right outermost wire anchors.

Beams 1.1 and 1.2 were reference beams, so Ni-Ti-Nb spirals were not used. In Beams 2.1, 2.2, 5.1, and 5.2, the activation of the Ni-Ti-Nb spirals was carried out before preloading the beams, which contained no preexisting cracks. In Beams 4.1 and 4.2, the beams were pre-cracked by a shear force of around 18 kN (see Table 1), which represents approximately 98% of the maximum shear strength of the reference beams. In Beams 3.1 and 3.2, the Ni-Ti-Nb spiral was placed and fixed around the beams but not activated. The beams were then tested to collapse in Tests 3.1a and 3.2a (note in Fig. 5 that the spiral wire is depicted with a curvature, indicating that the strengthening material had not

been activated). After the collapse, the Ni-Ti-Nb wire was activated, generating the recovery stress, then the beams were retested in Tests 3.1b and 3.2b.

3.5 Instrumentation and testing procedure

To monitor the behavior of the tested beam specimens, the applied load, the strains at discrete points in the reinforcement, and the displacements were measured using a load cell, strain gauges (see locations in Fig. 5), and magnetostrictive transducers. The strains in the longitudinal reinforcement were measured with three strain gauges (named GLONG) located in the midpoint and close to supports. The strains in the shear reinforcement (pseudo-spiral) were measured by means of strain gauges placed in central location of vertical link of each spiral (named GTR). The numbering used follows a sequential order from left to right in the frontal view. Video and photography equipment was also used to record the tests. All parameters were monitored continuously by the data acquisition system.

The tests were carried out under displacement control using a hydraulic actuator with a maximum load capacity of 100 kN. The supporting plates were 60 mm long in the direction of the longitudinal axis of the beam, and the loading plate was 105 mm wide. The load was applied by two cylinders with centers spaced 80 mm apart. A sliding pin bearing was placed at the west side and a fixed pin bearing was placed at the east side (Fig. 5). The displacement at the loading plate was monotonically increased until failure.

4. Results of experimental tests and discussion

4.1 Observed behavior and shear strength

All the tested beams failed in shear, as initially designed (see section 3.1), except for Beam 5.2 which failed in bending, although shear critical cracks had already developed in its two shear spans. Table 2 and Figs. 15–18 summarize the most important results. Table 2 shows for every beam, age of testing, compressive (f_{cm}) and splitting (f_{sp}) strength, maximum shear force (V_{test}) and mid-span deflections at that shear force (δ at V_{test}). The ratio between mid-span deflection at the maximum shear force and the beam span (δ/l) is an indicator of the ductility of the tested beams. Generally, displacement ductility in current codes is defined as the ratio of the peak displacement to the idealized yield displacement [35]. However, the ductility of SMA reinforced members based on this definition could be misleading, as Tazarv and Saiidi [35] pointed out, because the yield strain of SMA bars or wires is approximately five times higher than that of steel bars

resulting in a higher idealized yield displacement, thus lower calculated displacement ductility even though the displacement capacity of a SMA-reinforced member could substantially exceed that of a comparable conventional member. For that reason, Tazarv and Saiidi [35] proposed the use of the *drift ratio* for columns as ductility indicator, that is, the ratio of column lateral top displacement to the column height. For beams, the term δ/l would be the equivalent term.

The effectiveness of the proposed strengthening method can be shown by means of the increment of shear strength of a strengthened beam with respect to the shear strength of the non-strengthened beams. Therefore, the ratio between the shear strength (V_{test}) and average shear strength of non-strengthened beams, ($V_{no\ strength.}$) is calculated. The average value of non-strengthened beams, taken from beams 1.1 and 1.2, is $V_{no\ strength.} = 18.36$ kN. The effectiveness of the method is clearly shown since an average value of this ratio calculated of all strengthened beams of the experimental program is ($V_{test}/V_{no\ strength.} = 1.92$). Moreover, the higher ratios correspond to the beams strengthened with the pseudo-spiral with the pitch of 75 mm.

Table 2. Summary of test results.

Beam no.	Age at testing (days)	f_{cm} (MPa)	f_{sp} (MPa)	V_{test} (kN)	δ at V_{test} (mm)	δ/l (l/l)	$V_{test}/V_{no\ strength.}$
1.1 – Reference	49	41.4	3.2	18.30	1.59	1/479	-
1.2 – Reference	56	41.7	3.2	18.41	1.64	1/462	-
2.1 - S ϕ 3/100/UCR/A	63	41.9	3.2	35.41	4.26	1/178	1.93
2.2 - S ϕ 3/100/UCR/A	68	42.1	3.2	35.95	4.94	1/154	1.96
3.1a - S ϕ 3/100/UCR/NA	102	42.6	3.3	18.23	1.67	1/456	-
3.1b - S ϕ 3/100/COL/A	130	42.8	3.3	27.14	3.46	1/220	1.48
3.2a - S ϕ 3/100/UCR/NA	102	42.6	3.3	21.47	1.69	1/450	-
3.2b - S ϕ 3/100/COL/A	116	42.7	3.3	35.21	3.83	1/198	1.92
4.1 - S ϕ 3/100/PCR/A	175	43.0	3.3	34.35	3.82	1/199	1.87
4.2 - S ϕ 3/100/PCR/A	182	43.0	3.3	35.60	4.10	1/185	1.94
5.1 - S ϕ 3/075/UCR/A	263	43.2	3.4	37.04	3.82	1/199	2.02
5.2 - S ϕ 3/075/UCR/A	272	43.2	3.4	41.82	6.95	1/109	2.28

Fig. 15 shows the deflection-shear force curves of the reference beams (1.1 and 1.2), the beams with the non-activated spiral (3.1a and 3.2a), the strengthened beams with wire pitch equal to 100 mm (2.1 and 2.2), and the strengthened beams with wire pitch equal to 75 mm (5.1 and 5.2). It can be seen that when the pseudo-spiral is placed around the beam without being activated, it is negligibly effective, thus the results for Beams 3.1a and 3.2a are very similar to the results for the reference beams. However, when the spiral is activated (Beams 2.1, 2.2, 5.1, and 5.2), the strengthening method is clearly effective in all cases, providing the highest shear strengths with the reduced-pitch (75 mm) spiral.

The crack patterns in the reference beams and in the strengthened beams that failed in shear were very similar. Figure 16 shows the crack patterns of all tested beams just after the maximum applied load. For clarity, only one side of the beam, the critical one, is depicted. For most of the tested beams, a typical shear crack pattern is detected, with a first branch and second branch of the critical shear crack. The first branch developed inclined with an average value of 47° , but with a relatively high scatter from around 30° to 60° , from the lower part of the beam to the vicinity of the neutral axis. A second branch developed from the tip of the first branch to the point of load application, crossing the compression chord.

Note that the behavior of beam 5.2 (bending failure) differs from that of the beam 5.1 (shear failure). This may be due to the fact that the starting point of the critical shear crack in the beam 5.2 was forced by the small groove in the vertical of the GTR 7 (see figure 16 5-2), relatively close to the point of load application. For this reason, in the two sides of the beam 5.2, direct struts can be developed connecting the load application point to the support without passing through cracked concrete, enhancing the arch effect and thus increasing the shear strength. However, in beam 5.1, the critical shear crack developed closer to the support. Since the shear force needed to reach the ultimate bending moment at the beam is 40.5 kN, beam 5.2 failed in bending with a shear force equal to 41.82 kN (see table 2).

Regarding to the spiral wire reinforcement, no slippage around the corners of the cross section, or damage in the wire anchorages, was detected.

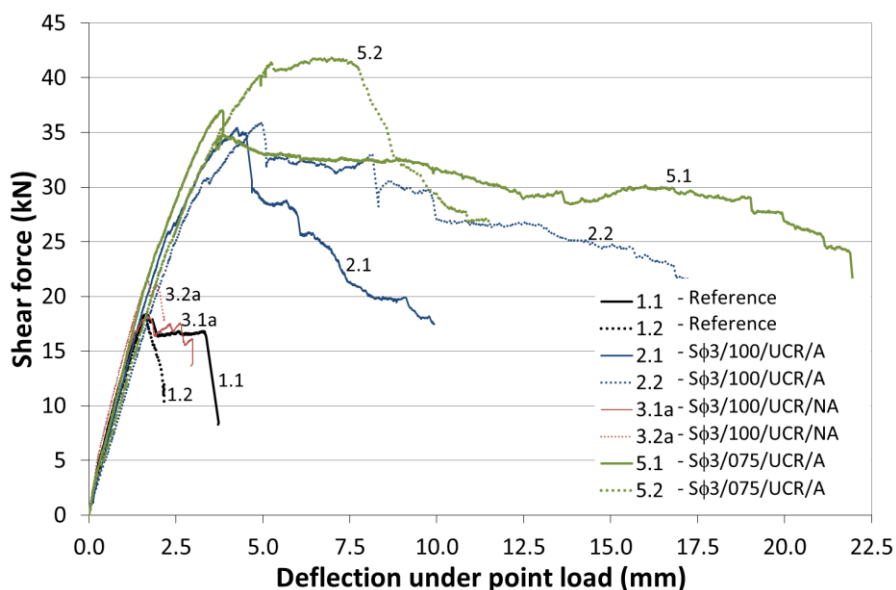


Fig. 15. Load vs. deflection for reference beams (1.1 and 1.2), strengthened beams with pitch equal to 100 mm (2.1 and 2.2), beams with the spiral un-activated (3.1a and 3.2a), and strengthened beams with pitch equal to 75 mm (5.1 and 5.2).

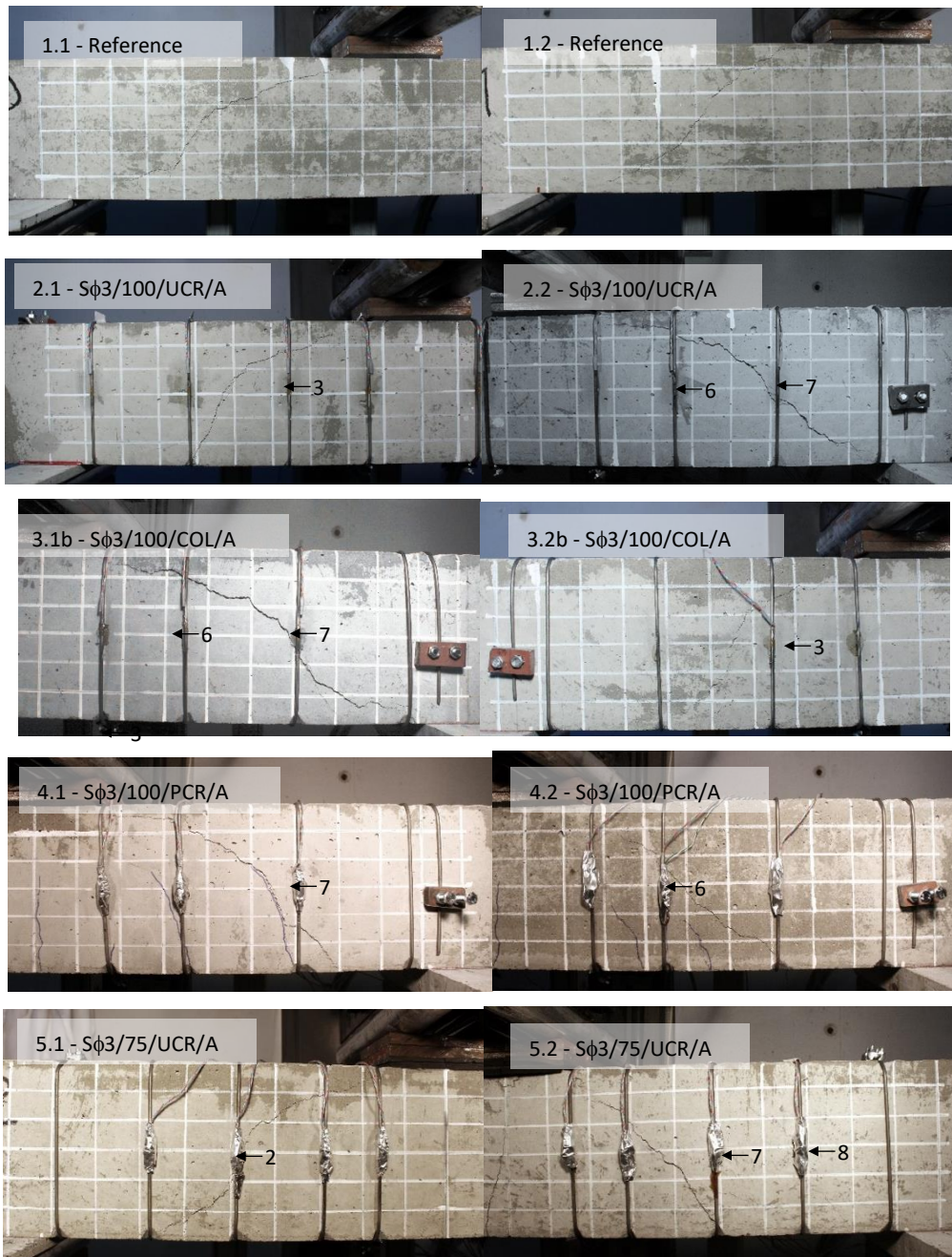


Fig. 16. Photographs of beam specimens just after their maximum load was achieved, with the numbering of the strain gauges (GTR) of the vertical links crossing the critical cracks.

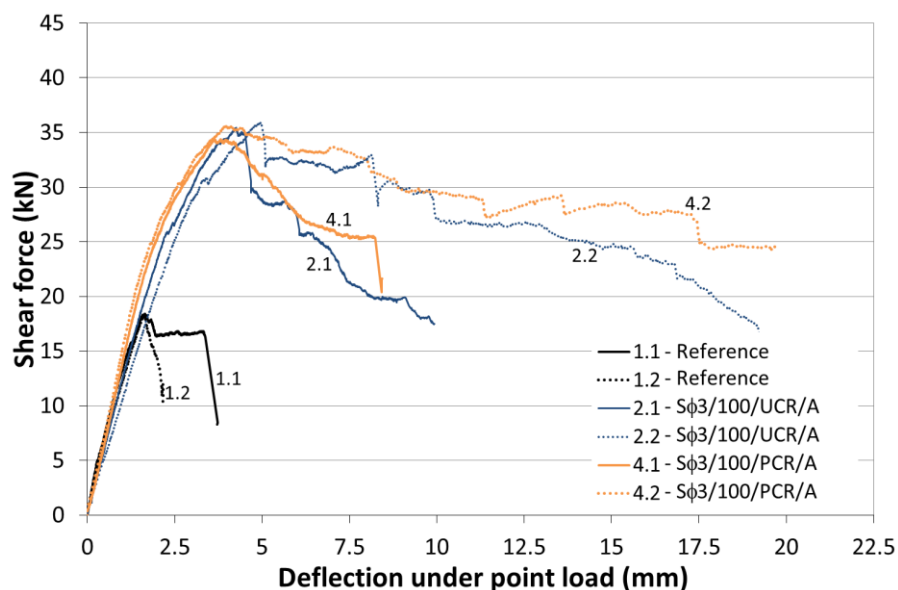


Fig. 17. Load vs. deflection for reference beams (1.1 and 1.2), strengthened beams with pitch equal to 100 mm (2.1 and 2.2) and strengthened beams after pre-cracking with pitch equal to 100 mm (4.1 and 4.2).

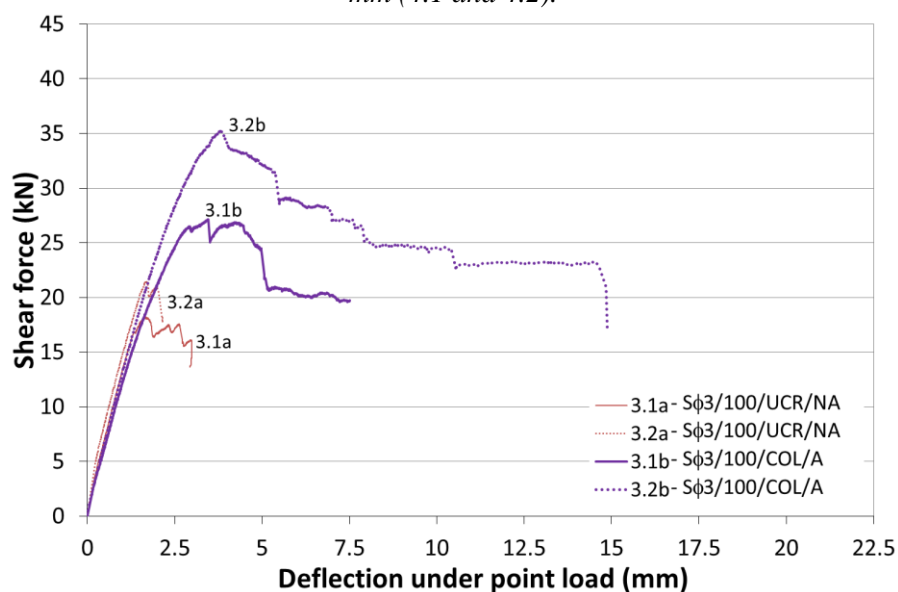


Fig. 18. Load vs. deflection for reference beams with the spiral un-activated (3.1a and 3.2a) and the same beams with the spiral activated after the first collapse (3.1b and 3.2b).

Fig. 17 compares the deflection-shear force curves for the reference beams (1.1 and 1.2), strengthened beams with pitch equal to 100 mm and activated without initial cracking (2.1 and 2.2), and beams with similar strengthening activated with preexisting shear cracking (4.1 and 4.2). In the latter case, the beams had previously been loaded to approximately 98% of the maximum shear force determined for the reference beams, and the alloy was activated afterwards. The behavior of the beams, in terms of maximum shear force and deflection, is very similar, and pre-cracking the beams by shear loading

does not affect the results. It must be highlighted that the shear cracks developed during the pre-load tests were almost closed during the unloading and subsequent activation of the SMA wires before performing the second test. For this reason, these pre-cracked beams behaved in a very similar way to the intact ones.

Two beams were loaded until collapse (3.1a and 3.2a) and then they were activated and tested again (3.1b and 3.2b). The results (Table 2 and Fig. 18) show that the strengthening method was able to increase the shear strength of the beam even after it had already collapsed, without conducting any additional rehabilitation work. Beam 3.2b showed a very similar response to the other strengthened specimens with the same wire pitch (2.1, 2.2, 4.1, and 4.2), although Beam 3.1b exhibited a lower degree of shear strength increase. Note however, that Beam 3.1a had been observed to suffer damage levels higher than those incurred by Beam 3.2a after the initial collapse. As can be seen in Fig. 18, the tested Beam 3.1a was more damaged with a higher reduction of stresses and higher post-peak deflections, after the precracking, than Beam 3.2a. As a consequence, the more damage caused in Beam 3.1a implied a lower shear strength of the test 3.1b compared to test 3.2b.

Fig. 19 shows the strain measured in the longitudinal reinforcement for four representative tests. It can be seen that in Beam 5.2 (which failed in bending), the longitudinal reinforcement yielded at mid span (Gauge GLONG.02, see Fig. 5). However, in the other beams (Beams 2.2 and 4.2), the longitudinal reinforcement did not yield at mid-span, but instead yielded close to the support in the shear span, near where the critical crack developed, at a load close to failure.

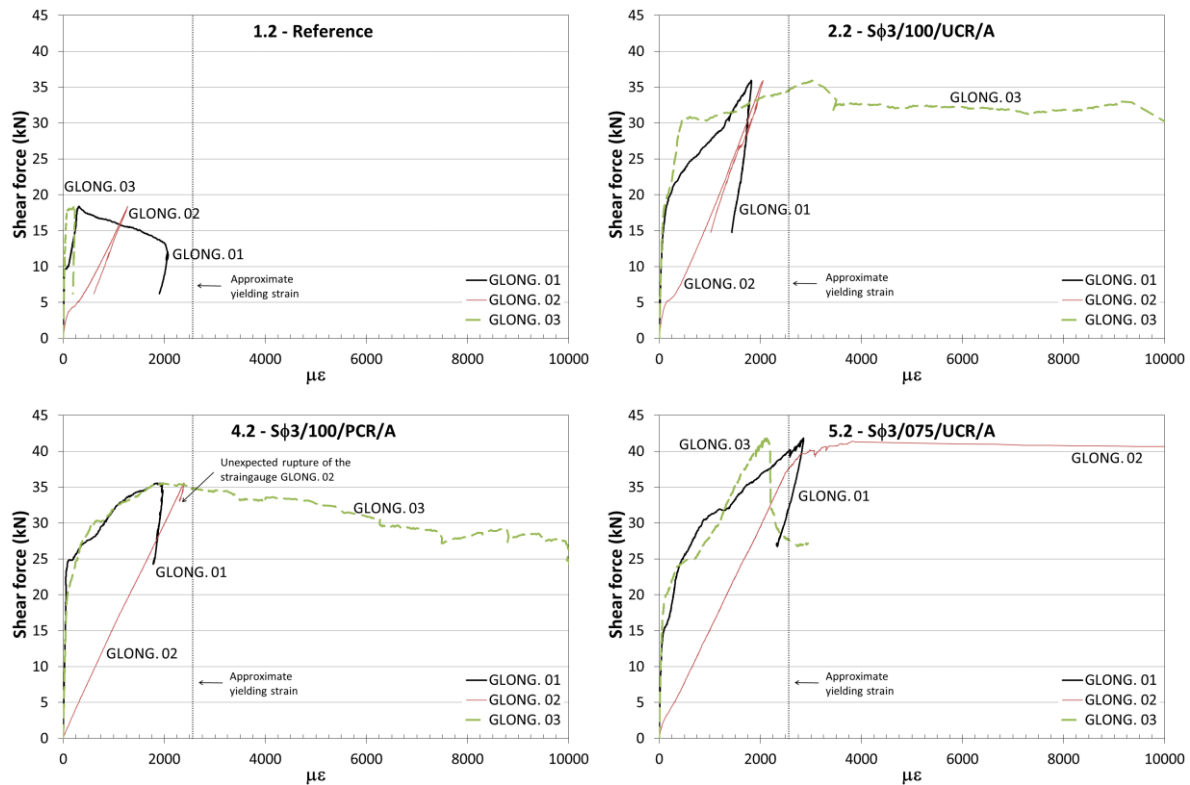


Fig. 19. Strains measured in the longitudinal reinforcement of Beams 1.2, 2.2, 4.2, and 5.2.

The strain measured in the vertical segments of the Ni-Ti-Nb pseudospiral are represented for a selection of representative beams in Fig. 20. For clarity, only the strain measured in the gauges located in the critical span are represented. The strain in the vertical links remains negligible until the shear cracks propagate. At failure, different strain values were measured across the tested beams. Table 3 shows the recovery stress (σ_R) after activation with the initial imperfection considered for each beam (i_o) and the strains ($\mu\epsilon$) measured at the maximum shear force for the links crossing the shear-critical crack (Fig. 16). Note that the Ni-Ti-Nb wires were prestrained with initial stress, after imperfect installation, with a minimum value of 415 MPa, as can be seen in table 3. These values were indirectly obtained considering the initial imperfection (i_o) of each spiral link and applying the performance curve shown in Fig. 13b. Moreover, taking into account the tangent modulus of elasticity of Ni-Ti-Nb after the generation of recovery stresses ($E = 25$ GPa), the increase of stress in the Ni-Ti-Nb spiral has been calculated from the measured strains at the maximum load ($\Delta\sigma_\epsilon = E \cdot \epsilon$). The obtained stress increments for each beam are also shown in Table 3. The final stress for the maximum load is given in the last column ($\sigma_R + \Delta\sigma_\epsilon$). Note that there is not bonding between the shear reinforcement and the concrete, except for the friction concentrated at the corners of the cross-section of the beams.

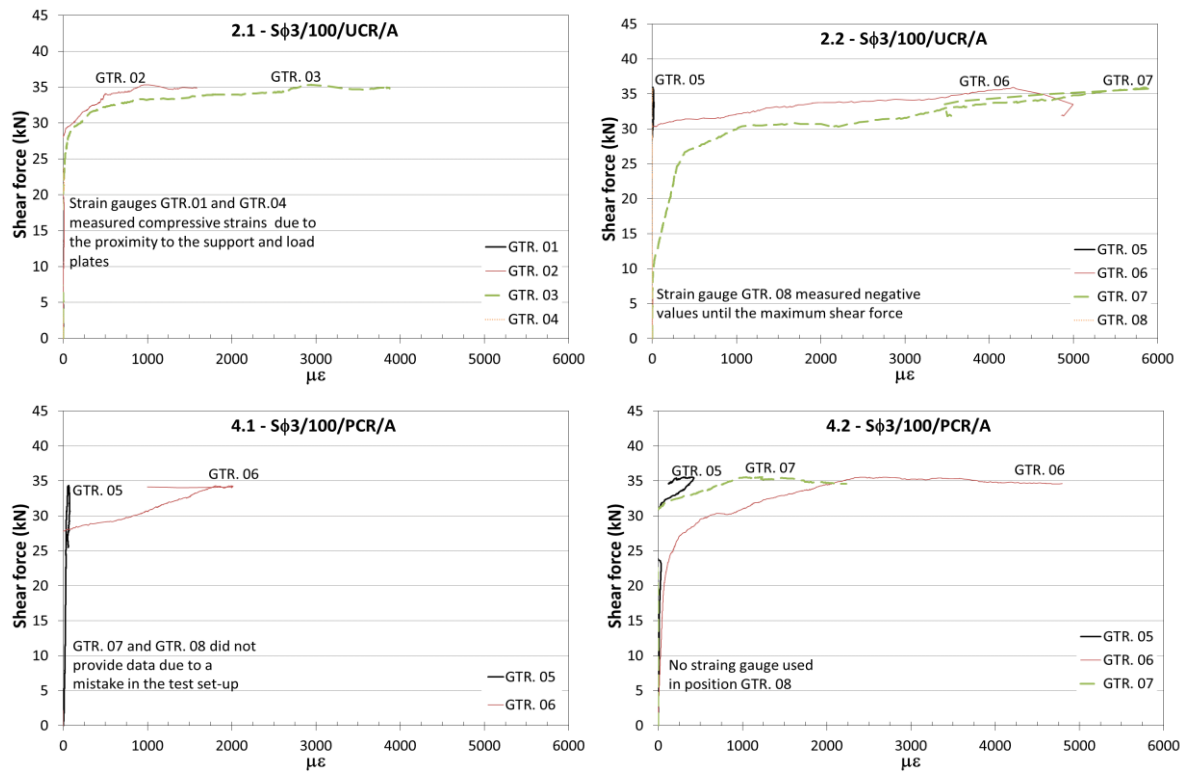


Fig. 20. Strains measured in the vertical links of the spirals in beams 2.1, 2.2, 4.1 and 4.2.

Table 3. Recovery stresses after activation with initial imperfection, strains measured at the maximum shear force for the links crossing the shear-critical crack and total stresses developed

BEAM	i_0 (%)	σ_R (MPa)	Gauges in links crossing the critical crack				Average $\mu\epsilon$	$\Delta\sigma_\varepsilon$ (MPa)	$\sigma_R + \Delta\sigma_\varepsilon$ (MPa)
			GTR	$\mu\epsilon$	GTR	$\mu\epsilon$			
2.1	1.83	417	3	3148	-	-	3148	79	496
2.2	1.20	432	6	4645	7	4675	4660	116	548
3.1b	1.03	435	6	#	7	#	#	70*	505
3.2b	1.37	428	3	2016	-	-	2016	50	479
4.1	0.94	436	7	1968	-	-	1968	49	485
4.2	1.90	415	6	2686	-	-	2686	67	482
5.1	1.14	433	2	2371	-	-	2371	59	492
5.2**	1.00	435	7	-	-	-	-	-	-

No values were recorded due to error in set-up
*Average value
** This beam failed in bending, so the measurements are not significant

4.2 Comparison of the experimental results with the Compression Chord Capacity Model predictions

The Compression Chord Capacity Model (CCCM) [36] was recently presented as a design-oriented model for the shear strength of reinforced concrete (RC) and prestressed concrete (PC) beams. It is a simplification of the Multi-Action Model [37] which, based

on classic mechanics, proposes explicit equations for the different shear transfer actions.

On the Multi-Action Shear Model, the shear force is transferred through:

- the uncracked concrete in the compression chord,
- residual tensile stresses in the cracked concrete web,
- the dowel effect of the longitudinal reinforcement,
- the shear reinforcement, if it exists.

The use of explicit equations for each shear resisting action may result in an approach too complex for daily engineering practice. For this reason, a transparent simplification was carried out [36], under the premise that the shear transferred by the compression chord is the main resisting action in the considered failure state. The main expressions governing the shear strength are summarized in Table 4 for the particular case of RC beams with rectangular cross sections. See Reference [36] for a detailed description of each expression and all factors.

Note that the shear strength of structural concrete members is still an open topic in scientific research (see, for instance, the 7 papers related to shear strength published recently in the same journal issue, including reference [38]), and, thus, other shear models could have been used to predict the shear strength of the strengthened beams. That said, even though the CCCM was not initially derived specifically as a model taking into account externally added strengthening reinforcement, it may be used without any problem and, additionally, it explicitly accounts for the portion of the shear resisted by the concrete confined within the stirrups in the compression chord, through the term Δ_{Vcu} (Eqs. (4) and (7)).

Table 4. Summary of basic CCCM formulation particularized for reinforced concrete beams with rectangular cross-sections

Equations	Expressions
Shear strength	$V_{Rd} = V_{cu} + V_{su} \leq V_{Rd,max}$ (1)
Strut crushing	$V_{Rd,max} = \alpha_{cw} b z v_1 f_{cd} \frac{\cot\theta + \cot\alpha}{1 + \cot^2\theta}$ (2)
Concrete contribution	$V_{cu} = 0.3 \zeta \frac{x}{d} f_{cd}^{2/3} b d$ (3)
Shear reinforcement and concrete contribution increase due to confinement	$V_{su} = \frac{A_{sw}}{s} f_{ywd} (d - x) \sin\alpha (\cot\theta + \cot\alpha) (1 + \Delta_{Vcu})$ (4)
Factors	Expressions
Size and slenderness effect	$\zeta = \frac{2}{\sqrt{1 + \frac{d_0}{200}}} \left(\frac{d}{a}\right)^{0.2}$ (5)
Relative neutral axis depth	$\frac{x}{d} = \alpha_e \rho_l \left(-1 + \sqrt{1 + \frac{2}{\alpha_e \rho_l}}\right)$ (6)
Non-dimensional confinement factor	$\Delta_{Vcu} = \zeta \frac{x}{d}$ (7)
Crack inclination	$\cot\theta = \frac{0.85d}{d-x} \leq 2.5$ (8)

Table 5. Predictions by the CCCM and EC 2.

Beam no.	$f_{cm,cyl}$ (MPa)	f_s (MPa)	V_{test} (kN)	Compression Chord Capacity Model						Eurocode 2		
				Prediction			Design			$V_{Rd,c}$ (kN)	$V_{Rd,s}$ (kN)	V_{test}/V_{Rd}
				V_{cu} (kN)	V_{su} (kN)	V_{Rd} (kN)	V_{test}/V_{Rd}	V_{Rd} (kN)	V_{test}/V_{Rd}			
1.1 – Reference	37.3	-	18.30	16.85	-	16.85	1.09	16.85	1.09	15.34	-	1.19
1.2 – Reference	37.5	-	18.41	16.92	-	16.92	1.09	16.92	1.09	15.37	-	1.20
2.1 – S ϕ 3/100/UCR/A	37.7	496	35.41	16.96	12.64	29.60	1.20	28.81	1.23		20.56	1.72
2.2 – S ϕ 3/100/UCR/A	37.9	548	35.95	17.01	13.97	30.88	1.16	28.86	1.25		22.73	1.58
3.1a – S ϕ 3/100/UCR/NA	38.3	-	18.23	17.12	-	17.12	1.06	17.12	1.06	15.48	-	1.18
3.1b – S ϕ 3/100/COL/A	38.5	505	27.14	17.17	12.86	30.03	0.90	29.01	0.94		20.94	1.30
3.2a – S ϕ 3/100/UCR/NA	38.3	-	21.47	17.12	-	17.12	1.25	17.12	1.06	15.48	-	1.39
3.2b – S ϕ 3/100/COL/A	38.4	479	35.21	17.14	12.20	29.34	1.20	28.99	1.21		19.86	1.77
4.1 – S ϕ 3/100/PCR/A	38.7	485	34.35	17.21	12.36	29.57	1.16	29.05	1.18		20.13	1.71
4.2 – S ϕ 3/100/PCR/A	38.7	482	35.60	17.21	12.29	29.50	1.21	29.05	1.23		20.01	1.78
5.1 – S ϕ 3/075/UCR/A	38.9	492	37.04	17.25	16.61	33.86	1.09	32.94	1.12		27.49	1.35
5.2 – S ϕ 3/075/UCR/A	38.9	505	41.85	17.25	17.05	34.30	1.22	32.94	1.27		28.22	1.48
						Average	1.14		1.16			1.47
						Standard deviation	0.09		0.10			0.23
						Coef. of Variation (%)	8.4		8.7			16.0

The predictions made by the CCCM are presented in Table 5. The concrete compression strength of the cylinder specimens is taken equal to $0.9 \cdot f_{cm}$ [28]. The compression strength varied slightly depending on the age of the specimen at testing, insignificantly affecting the concrete contribution V_{cu} (Table 5). The average value of x , the neutral axis depth, is 49 mm according to Eq. (6). It can be seen in Fig. 16 that this is a very close estimation of the separation between the first branch of the critical crack (more vertical) and the second branch (more horizontal, through the compression chord). For reference, in Fig. 16 the spacing of the horizontal guidelines painted on the beam specimens is 25 mm.

No partial safety coefficients were used in the calculations presented in Table 5. The yield strength of the material, f_{ywd} , was substituted by the stress in the spiral at failure (see f_s in column 3 in table 5), as carefully commented previously. The pitch or spacing of the vertical segments of the spiral was constant in the tested beams (nominally 100 mm or 75 mm), except for the vertical segments closest to the loading plate (75 mm and 50 mm, see Fig. 5). For the application of the CCCM, the nominal spacing has been taken into account, as this is the distance between the segments in the first branch of the critical crack (Fig. 21), and this is the value required to obtain V_{su} (Table 5).

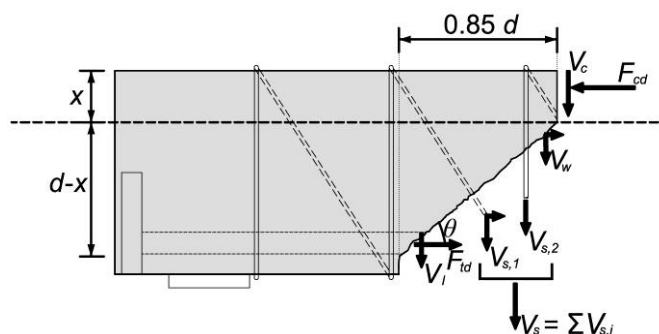


Fig. 21. First branch of the critical crack and stirrup contribution.

The predictions given by the model without any modification with respect to the procedure established to evaluate internal reinforcement are excellent (see Table 5, CCCM prediction), with an average value of the ratio V_{test}/V_{Rd} equal to 1.14 and a coefficient of variation of 8.4 %. The average value of the ratio V_{test}/V_{Rd} is similar to the ratios for the shear strength of 784 RC beams without stirrups ($V_{test}/V_{Rd} = 1.17$) and 170 RC beams with stirrups ($V_{test}/V_{Rd} = 1.16$) [36]. Note that only the prediction for beam 3.1b - S ϕ 3/100/COL/A is unsafe ($V_{test}/V_{Rd} < 1.0$). As previously commented in section 4.1, the beam had previously suffered a very high damage level in test 3.1a and, in real engineering, this beam specimen would have not probably been strengthened after its collapse. Note that having non-activated SMA in place (beams 3.1a – S ϕ 3/100/UCR/NA and 3.2a – S ϕ 3/100/UCR/NA) did not increase the shear strength nor the predictions. However activated SMA for pre-cracked and un-cracked sections almost doubled the shear test results, irrespective of the pre-cracking.

The predictions when using the current Eurocode 2 (EC 2) [39] are also presented in Table 5. Note that EC 2 presents two different models for elements without and with stirrups: an empirical equation for members without stirrups, and a variable angle truss model without concrete contribution for elements with stirrups. It must be noted that EC2

model is not intended for calculating the shear strength of externally strengthened beams. The results are quite conservative and present a high scatter, with an average value of the ratio V_{test}/V_{Rd} equal to 1.47 and a coefficient of variation of 16.0 %.

Once it has been observed that the predictions of the shear strength by the CCCM satisfactorily correlate with the experimental results, some simplifications have been performed for design purposes. It is suggested to use an initial stress value after activation of 415 MPa (value corresponding to an initial imperfection of 1.9 %) and an average increase of stress at failure of 50 MPa. Both proposed design values are conservative (see figure 13.b and table 5). Note that, in the authors' opinion, an initial imperfection of 1.9 % is an upper boundary, because the greater the depth of the beam, the less imperfection will be produced during the assembly process. The use of small scale members make it more difficult to place the wire around the beam. Note also that an increase of the tensile stress of 50 MPa is related to a strain equal to 0.002 (see Table 3), similar to the strain before failure assumed for internal steel shear reinforcement by different codes (e.g. EC 2 [39] and EHE 08 [28], among others).

The average obtained values of the V_{test}/V_{Rd} ratios (Table 5) using the above-mentioned design values (columns ninth and tenth in Table 5) is 1.16 and the coefficient of variation is 8.7 % Therefore, this approach is adequate for the design of the strengthening.

5. Conclusions

An experimental program assessing the possibility of strengthening shear-critical beams using a shape memory alloy relying on the shape memory effect has been presented. The experimental results show a promising performance of the proposed technology, which increased both the shear strength of the retrofitted beams and the deflection at failure. Furthermore, the tests have shown that pre-cracked beams, having been loaded to approximately 98% of their maximum shear force and actively strengthened by means of the proposed technology, perform similar to beams strengthened prior to cracking. The effectiveness of this shear strengthening method is shown, since an increment in shear strength of 92% has been achieved for the strengthened beams related to those non-strengthened. The experimental campaign carried out has been a first phase of a broader experimental program and it has confirmed the effectiveness of the new methodology of active shear strengthening of RC beams

using SMAs. These results have been the basis to plan other strengthening configurations for another experimental campaign.

This research was planned as a proof-of-concept experimental program to demonstrate the feasibility of using externally placed SMAs wires to increase the shear strength of RC members, but more research is still required. The cost of Ni-Ti-Nb is very high, but recent research on iron-based shape memory alloys envisages the application of cheaper shape memory alloys with very similar behavior. Despite the high cost of Ni-Ti-Nb, the amount of material needed is small and should be placed only in critical regions of the beams, so this application promises a very interesting technology for the strengthening of key civil infrastructures.

The shear strength of the tested beam specimens was compared with the predictions made by the Compression Chord Capacity Model (CCCM) and Eurocode 2, using measured values of strains in the tests. The shear strength predictions by the model included in Eurocode 2 [39] are excessively conservative. However, the CCCM was perfectly able to predict the shear strength of the reference and strengthened beams presented in this paper. Furthermore, design values for the recovery stresses and the increment of stresses at failure for the external pseudo-spirals are proposed.

Notations

- a shear span, the distance from the support to the resultant of the loads producing shear at that support.
- b width of the cross-section.
- d effective depth of the cross-section.
- f_{cd} is the design value of concrete compressive strength.
- f_{ck} characteristic compressive strength of concrete.
- f_{cm} mean compressive strength of concrete using 150-mm cubes.
- $f_{cm,cyl}$ mean compressive strength of concrete using 150 x 300 mm cylinders, considered equal to $0.9f_{cm}$.
- f_s stress in the spiral at failure, equal to $\sigma_R + \Delta\sigma_\varepsilon$
- f_{sp} mean splitting strength of concrete using 150 mm x 300 mm cylinders.

- f_y mean yield strength of the reinforcement.
- f_{ywd} design yield strength of the shear reinforcement.
- f_u failure strength of the reinforcement.
- h overall depth of a cross-section.
- i_0 percentage of initial imperfection of the wires.
- s spacing of the stirrups.
- x neutral axis depth of the cracked section, obtained assuming zero concrete tensile strength.
- z inner lever arm. In the shear analysis of reinforced concrete members without axial force, the approximate value $z \approx 0.9d$ may normally be used.
- A_f austenite finish temperature.
- A_s austenite start temperature.
- A_{sw} cross-sectional area of the shear reinforcement.
- E_{cm} secant modulus of elasticity of concrete, $E_{cm} = 22000(f_{cm}/10)^{0.3} \neq 39 \text{ GPa}$.
- E_s modulus of elasticity of reinforcing steel.
- M_f martensite finish temperature.
- M_s martensite start temperature.
- V_{cu} concrete contribution to the shear resistance of the member.
- $V_{no \text{ strength}}$ average shear strength of reference beams 1.1 and 1.2.
- V_{Rd} design shear resistance of the member.
- $V_{Rd,max}$ design value of the maximum shear force which can be sustained by the member, limited by crushing of the struts.
- V_{su} contribution of internal or external shear reinforcement to the shear resistance of the member.
- V_{test} experimental shear strength of a tested beam.

- α angle between shear reinforcement and the beam axis perpendicular to the shear force in Eq. (4).
- α_{cw} coefficient taking account the state of the stress in the struts: $\alpha_{cw} = 1$ for non prestressed structures; $\alpha_{cw} = 1 + \sigma_{cp}/f_{cd}$ for $0 \leq \sigma_{cp} \leq 0.25f_{cd}$; $\alpha_{cw} = 1.25$ for $0.25f_{cd} < \sigma_{cp} \leq 0.50f_{cd}$; and $\alpha_{cw} = 2.5(1 - \sigma_{cp}/f_{cd})$ for $0.50f_{cd} < \sigma_{cp} \leq f_{cd}$.
- α_e modular ratio, $\alpha_e = E_s/E_{cm}$.
- δ/l ratio between mid-span deflection at the maximum shear force and the beam span.
- ν_1 strength reduction factor for concrete cracked in shear, $\nu_1 = 0.6$ for $f_{ck} \leq 60$ MPa and $\nu_1 = 0.9 - f_{ck}/200$ for $f_{ck} > 60$ MPa.
- θ angle between the concrete compression strut and the beam axis perpendicular to the shear force, given by Eq. (8).
- ρ_l longitudinal tensile reinforcement ratio referred to the effective depth d and the width b .
- σ_R recovery stress taking into account the initial imperfection i_0 .
- ζ combined size and slenderness effect factor, given by Eq. (5).
- Δv_{cu} non-dimensional confinement factor which considers the increment of the shear resisted by the concrete caused by the stirrup confinement in the compression chord, see Eq. (7).
- $\Delta \sigma_\varepsilon$ stress increase from the recovery stress in the Ni-Ti-Nb wires at shear failure of the strengthened beams.

Conflict of interest

None

Acknowledgments

This research was developed in the framework of projects BIA2015-64672-C4-3-R (AEI / FEDER, UE) and BIA2012-31432 (MINECO / FEDER, UE). The authors also want to thank Dr. Kustov and his coworkers at the University of the Balearic Islands for his help in determining the phase transformation temperatures. The beam specimens were cast at the Pastor precast concrete plant, located in Santa Margalida (Mallorca, Spain). The authors acknowledge their help and assistance.

References

- [1] Lin F, Hua J, Dong Y. Shear Transfer Mechanism of Concrete Strengthened with External CFRP Strips. *J Compos Constr* 2017;21. doi:10.1061/(ASCE)CC.1943-5614.0000751.
- [2] Chalioris CE, Thermou GE, Pantazopoulou SJ. Behaviour of rehabilitated RC beams with self-compacting concrete jacketing - Analytical model and test results. *Constr Build Mater* 2014;55:257-73. doi:10.1016/j.conbuildmat.2014.01.031.
- [3] Foster RM, Morley CT, Lees JM. Shear transfer across a diagonal crack in reinforced concrete strengthened with externally bonded FRP fabric. *Adv. Compos. Constr.* 2013, ACIC 2013 - Conf. Proc., Department of Engineering, University of Cambridge: 2013, p. 166-77.
- [4] Ruano G, Isla F, Pedraza RI, Sfer D, Luccioni B. Shear retrofitting of reinforced concrete beams with steel fiber reinforced concrete. *Constr Build Mater* 2014;54:646-58. doi:10.1016/j.conbuildmat.2013.12.092.
- [5] Ferreira D, Bairán JM, Marí A. Shear strengthening of reinforced concrete beams by means of vertical prestressed reinforcement. *Struct Infrastruct Eng* 2016;12:394-410. doi:10.1080/15732479.2015.1019893.
- [6] Yu T, Ma Q, Tian L. Test study on the resisting shear strengthening effect with external pre-stressed wire rope. *1st Int Conf Civ Eng Archit Build Mater CEABM* 2011 2011;243-249:5571-5. doi:10.4028/www.scientific.net/AMR.243-249.5571.
- [7] Czaderski C, Motavalli M, Winistorfer A. Prestressed shear strengthening of a box girder bridge with non-laminated CFRP straps. En: Empa, editor. *4th Int. Conf. FRP Compos. Civ. Eng. (CICE 2008)*, Zurich, Switzerland: 2008.
- [8] Motavalli M, Czaderski C, Pfyl-Lang K. Prestressed CFRP for Strengthening of Reinforced Concrete Structures: Recent Developments at Empa, Switzerland. *J Compos Constr* 2011;15:194-205. doi:10.1061/(ASCE)CC.1943-5614.0000125.
- [9] Leinenbach C, Lee WJ, Lis A, Arabi-Hashemi A, Cayron C, Weber B. Creep and stress relaxation of a FeMnSi-based shape memory alloy at low temperatures. *Mater Sci Eng A* 2016;677:106-15. doi:10.1016/j.msea.2016.09.042.
- [10] Shahverdi M, Michels J, Czaderski C, Motavalli M. Iron-based shape memory alloy strips for strengthening RC members: Material behavior and characterization. *Constr Build Mater* 2018;173:586-99. doi:10.1016/j.conbuildmat.2018.04.057.
- [11] Mas B, Cladera A, Ribas C. Experimental study on concrete beams reinforced with pseudoelastic Ni-Ti continuous rectangular spiral reinforcement failing in shear.

- Eng Struct 2016;127:759-68. doi:10.1016/j.engstruct.2016.09.022.
- [12] Otsuka K, Wayman CM. Shape Memory Materials. United Kingdom: Cambridge University Press; 1998.
- [13] Isalgue A, Auguet C, Grau R, Torra V, Cinca N, Fernandez J. Behavior of NiTi Wires for Dampers and Actuators in Extreme Conditions. *J Mater Eng Perform* 2015;24:3323-7. doi:10.1007/s11665-015-1607-x.
- [14] Mas B, Biggs D, Vieito I, Cladera A, Shaw J, Martínez-Abella F. Superelastic shape memory alloy cables for reinforced concrete applications. *Constr Build Mater* 2017;148. doi:10.1016/j.conbuildmat.2017.05.041.
- [15] Pereiro-Barceló J, Bonet JL. Ni-Ti SMA bars behaviour under compression. *Constr Build Mater* 2017;155:348-62. doi:10.1016/j.conbuildmat.2017.08.083.
- [16] Mas B, Cladera A, Ribas C. Fundamentos y aplicaciones piloto de las aleaciones con memoria de forma para su utilización en ingeniería estructural. *Hormigón y Acero* 2016;67:309-23. doi:10.1016/j.hya.2016.02.007.
- [17] Melton KN, Simpson J, Duerig TW. A new wide hysteresis NiTi based shape memory alloy and its applications. *Proc. Int. Conf. Martensitic Transform. ICOMAT-86*, 1986, p. 1053-8.
- [18] Melton KN, Proft JL, Duerig W. Wide hysteresis shape memory alloys based on the Ni-Ti-Nb system. *MRS Int'l. Mtg. Adv. Mats. Vol 9.*, 1989, p. 165-70.
- [19] Chen Q, Shin M, Andrawes B. Experimental study of non-circular concrete elements actively confined with shape memory alloy wires. *Constr Build Mater* 2014;61:303-11. doi:10.1016/j.conbuildmat.2014.02.076.
- [20] Dommer K, Andrawes B. Thermomechanical characterization of NiTiNb shape memory alloy for concrete active confinement applications. *J Mater Civ Eng* 2012;24:1274-82. doi:10.1061/(ASCE)MT.1943-5533.0000495.
- [21] Choi E, Choi D-H, Chung Y-S, DesRoches R. Seismic protection of lap-spliced RC columns using SMA wire jackets. *Mag Concr Res* 2012;64:239-52. doi:10.1680/mac.10.00181.
- [22] Cladera A, Weber B, Leinenbach C, Czaderski C, Shahverdi M, Motavalli M. Iron-based shape memory alloys for civil engineering structures: An overview. *Constr Build Mater* 2014;63:281-93. doi:10.1016/j.conbuildmat.2014.04.032.
- [23] Maruyama T, Kubo H. Ferrous (Fe-based) shape memory alloys (SMAs): properties, processing and applications. En: Yamauchi K, Ohkata I, Tsuchiya K, Miyazaki S, editores. *Shape Mem. superelastic Alloy. Technol. Appl.*, Cambridge (UK): Woodhead Publishing Limited; 2011, p. 141-59.
- [24] Lagoudas D. *Shape Memory Alloys*. Springer New York LLC; 2008. doi:10.1007/978-0-387-47685-8.
- [25] Desroches R, McCormick J, Delemont M. Cyclic Properties of Superelastic Shape Memory Alloy Wires and Bars. *J Struct Eng* 2004;130:38-46. doi:10.1061/(ASCE)0733-9445(2004)130:1(38).
- [26] AENOR, UNE-EN-12390-3. Testing hardened concrete - Part 3: Compressive strength of test specimens 2009.
- [27] AENOR, UNE-EN-12390-6. Testing hardened concrete - Part 6: Tensile splitting strength of test specimens 2010.

- [28] Comisión Permanente del Hormigón. Instrucción de Hormigón Estructural EHE-2008. Madrid: Ministerio de Fomento; 2008.
- [29] AENOR, UNE36065. Ribbed bars of weldable steel with special characteristics of ductility for the reinforcement of concrete 2011.
- [30] Kustov S, Salas D, Cesari E, Santamarta R, Van Humbeeck J. Isothermal and athermal martensitic transformations in Ni–Ti shape memory alloys. *Acta Mater* 2012;60:2578-92. doi:10.1016/j.actamat.2012.01.025.
- [31] De Corte W, Boel V. Effectiveness of spirally shaped stirrups in reinforced concrete beams. *Eng Struct* 2013;52:667-75. doi:10.1016/j.engstruct.2013.03.032.
- [32] Karayannis CG, Chalioris CE. Shear tests of reinforced concrete beams with continuous rectangular spiral reinforcement. *Constr Build Mater* 2013;46:86-97. doi:10.1016/j.conbuildmat.2013.04.023.
- [33] Yang K-H, Kim G-H, Yang H-S. Shear behavior of continuous reinforced concrete T-beams using wire rope as internal shear reinforcement. *Constr Build Mater* 2011;25:911-8. doi:10.1016/j.conbuildmat.2010.06.093.
- [34] Azimi M, Bagherpourhamedani A, Tahir MM, Bin Mohd Sam AR, Ma C-K. Evaluation of new spiral shear reinforcement pattern for reinforced concrete joints subjected to cyclic loading. *Adv Struct Eng* 2016;19:730-45. doi:10.1177/1369433216630371.
- [35] Tazarv M, Saiidi MS. Analysis , Design , and Construction of SMA-Reinforced FRP- Confined Concrete Columns. SMAR 2017 - Fourth Conf. Smart Monit. Assesment Rehabil. Civ. Struct., Zurich: 2017.
- [36] Cladera A, Marí A, Bairán JM, Ribas C, Oller E, Duarte N. The compression chord capacity model for the shear design and assessment of reinforced and prestressed concrete beams. *Struct Concr* 2016;17:1017-32. doi:10.1002/suco.201500214.
- [37] Marí A, Bairán J, Cladera A, Oller E, Ribas C. Shear-flexural strength mechanical model for the design and assessment of reinforced concrete beams. *Struct Infrastruct Eng* 2015;11:1399-419. doi:10.1080/15732479.2014.964735.
- [38] Cladera A, Marí A, Bairán J-M, Oller E, Ribas C. One-Way Shear Design Method Based on a Multi-Action Model. *Concr Int* 2017;39:40-6.
- [39] European Committee for Standardization. Eurocode 2: Design of Concrete Structures: Part 1: General Rules and Rules for Buildings. European Committee for Standardization; 2002.